Supporting Information

Regulating Ag-Cu Synergy Effect via Cu Doping Numbers to Boost CO_2 Electroreduction on Ag_{14} Nanoclusters

Along Ma,‡[a] Yonggang Ren,‡[b] Yang Zuo,[b] Jiaqi Zhao,[a] Shuo Zhang,*[a] Xiaoshuang Ma*[b] and Shuxin Wang*[a,b]

[a]*Key Laboratory of Optic-electric Sensing and Analytical Chemistry for Life Science, MOE, Shandong Key Laboratory of Biochemical Analysis, College of Chemistry and Molecular Engineering, Qingdao University of Science and Technology, Qingdao 266042, P. R. China.*

[b]*College of Materials Science and Engineering, Qingdao University of Science and Technology, Qingdao 266042, P. R. China.*

*Corresponding authors. E-mail: shuxin_wang@qust.edu.cn (Shuxin Wang), xiaoshuang_ma@qust.edu.cn (Xiaoshuang Ma) and zhangshuo@qust.edu.cn (Shuo Zhang).

‡These authors contributed equally to this work.

Notes: The authors declare no competing financial interest.

Table of Contents

Section 3. Supporting Table

Section 1. Synthesis, Characterization, Electrochemical measurements, and DFT calculations

I. Synthesis

Chemicals: All reagents were commercially available and used without further purification. Silver nitrate ($AgNO_3$, 98% metals basis), copper(II) nitrate trihydrate ($Cu(NO_3)_2 \cdot 3H_2O$, 98% metal basis), pentafluorothiophenol (PFBT, 99%), tris(*m*-methoxyphenyl)phosphine (P(Ph-*m*-OMe)$_3$, 98%), sodium borohydride ($NaBH_4$, 98%), methyl alcohol (CH_3OH, MeOH, HPLC grade), ethyl alcohol (CH_3CH_2OH, EtOH, HPLC grade), dichloromethane (CH_2Cl_2, DCM, HPLC grade) and *n*-hexane (C_6H_{14}, Hex, HPLC grade), were used to carry out the experiments. All glassware was thoroughly cleaned with aqua regia ($V_{HCl} : V_{HNO3} = 3:1$), rinsed with copious pure water, and then dried in an oven prior to use.

Synthesis of $Ag_{14}(SPhF_5)_{12}(P(Ph\text{-}m\text{-}OMe)_3)_4$ (Ag_{14}) NC: Typically, $AgNO_3$ (37.5 mg, 0.22 mmol) was first dissolved in a solvent mixture of 10 mL CH_3OH and 10 mL CH_2Cl_2. After stirring for 5 minutes, PFBT (40 μL, 0.30 mmol) and P(Ph-*m*-OMe)$_3$ (134 mg, 0.38 mmol) were sequentially added in turn, resulting in a color change from colorless to milky white to colorless. Following an additional 20 minutes of vigorous stirring, $NaBH_4$ (30 mg, 0.79 mmol), dissolved in 2 mL H_2O, was quickly introduced, causing the solution to gradually darken. The reaction mixture was maintained at room temperature for 12 hours to complete the formation of Ag_{14} NCs. Subsequently, the organic phase was centrifuged for 5 minutes at 8000 rpm. The precipitate was discarded, and the organic solvent was evaporated to obtain the crude Ag_{14} NCs. The crude product was washed three times with 15 mL of *n*-hexane. Yellow, block-like crystals were obtained by crystallizing the purified NCs in a 1:3 mixture of CH_2Cl_2 and CH_3OH over two days at approximately 4 °C. The yield is 37% based on the Ag element (calculated from the $AgNO_3$) for the synthesis of Ag_{14}.

Synthesis of $Ag_{14-x}Cu_x(SPhF_5)_{12}(P(Ph\text{-}m\text{-}OMe)_3)_4$ ($1 \leq x \leq 4$, $(AgCu)_{14}$-1) NC: The $Ag_{12}Cu_2$ NCs were synthesized using a methodology analogous to that employed for the Ag_{14} NCs. Specifically, $AgNO_3$ (37.5 mg, 0.22 mmol) and $Cu(NO_3)_2 \cdot 3H_2O$ (8.9 mg, 0.037 mmol) were added to a solvent mixture comprising 10 mL CH_3OH and 10 mL CH_2Cl_2 under vigorous stirring. After stirring for 5 minutes, PFBT (40 μL, 0.30 mmol) and P(Ph-*m*-OMe)$_3$ (134 mg, 0.38 mmol) were sequentially introduced, resulting in a color change from colorless to yellow to white. After 20 minutes, a solution of $NaBH_4$ (30 mg, 0.79 mmol) dissolved in 2 mL EtOH was rapidly added, causing the solution to gradually darken. The reaction was maintained at room temperature for 12 hours to facilitate the formation of the **$(AgCu)_{14}$-1** NCs. Following the reaction completion, the reaction solution was centrifuged for 5 minutes at 8000 rpm. The supernatant was discarded, and the precipitate was retained for further processing. The precipitate was washed three times with CH_3OH to obtain pure **$(AgCu)_{14}$-1** NCs. Yellow, block-like crystals were obtained by crystallizing the purified NCs in a 1:3 mixture of CH_2Cl_2 and CH_3OH over two days at approximately 4 °C. The yield is 33% for **$(AgCu)_{14}$-1** based on the Ag element (calculated from the $AgNO_3$).

Synthesis of $Ag_{14-x}Cu_x(SPhF_5)_{12}(P(Ph\text{-}m\text{-}OMe)_3)_4$ ($1 \leq x \leq 6$, $(AgCu)_{14}$-2) NCs: Based on the synthesis method of **$(AgCu)_{14}$-1** NCs, **$(AgCu)_{14}$-2** NCs were synthesized after increasing the amount of Cu salt to 21.5 mg (0.089 mmol). The yield of **$(AgCu)_{14}$-2** was approximately 37%, based on the Ag element (calculated from $AgNO_3$).

II. Characterization

Ultraviolet-visible spectroscopy (**UV-vis**): The UV-vis measurements in this study were recorded on an

Agilent Cary 5000 UV-Vis-NIR spectrophotometer. All crystal samples were dissolved in CH_2Cl_2 for spectrum measurements.

X-ray photoelectron spectroscopy (**XPS**): The XPS measurements were performed on ESCALAB XI+ configured with a monochromated $Al_{K\alpha}$ (1486.8 eV) 150W X-ray source, 0.5 mm circular spot size, a flood gun to counter charging effects, and the analysis chamber base pressure lower than 1 $x10^{-9}$ mbar, data were collected with FAT = 20 eV. The crystal particles of **Ag_{14}**, **$(AgCu)_{14}$-1**, and **$(AgCu)_{14}$-2** were adhered to packaging tape for testing, and a small amount of carbon was added to assist with data correction.

Scanning electron microscope-energy dispersive spectrometer (**SEM-EDS**): SEM-EDS was conducted on HITACHI Regulus 8100. The crystal particles of **Ag_{14}**, **$(AgCu)_{14}$-1**, and **$(AgCu)_{14}$-2** were tested by sticking on a conductive adhesive with an accelerating voltage of 0.1-30 kV.

Electrospray ionization mass spectrometry (**ESI-MS**): ESI-MS measurements were carried out on a Bruker micro TOF-Q system in positive or negative ion mode in the range m/z = 1000-6000. To prepare the ESI sample, clusters were dissolved in CH_2Cl_2/CH_3OH (V/V = 1 : 3).

X-ray crystallography:

Data collection: The data collections for single crystal X-ray diffraction (SC-XRD) were carried out on a Bruker D8 Quest at 170 K, using a Mo-Kα radiation (λ = 0.71073 Å).

Structure solution: The structures were solved by using the structure solution program ShelXT with the Intrinsic Phasing method in the OLEX2 software.

Structure Refinement: Refinements were performed on F^2 anisotropically for all the non-hydrogen atoms by the full-matrix least-squares method using the SHELXL program in Olex2 software. And all the hydrogen atoms were set in geometrically calculated positions and refined isotopically using a riding model.

Refinement Details of Ag_{14}: The methoxy group (C-O) exhibited disorder resolved by splitting into two orientations (C157-O3/C155-O11) with refined occupancy ratios of 0.602 : 0.398. The disordered carbon atom (C) in the phosphine ligand was modeled as two split positions (C37/C39) with an occupancy ratio of 0.68 : 0.32. Geometrical restraints were applied to maintain chemically reasonable bond lengths. Anisotropic displacement parameters (ADPs) of overlapping atoms were constrained using SIMU and RIGU instructions to ensure physically meaningful thermal motion correlation.

Refinement Details of $(AgCu)_{14}$-1: Methoxy group disorder (C-O) was modeled as two split orientations (C19A-O11A/C19B-O11B) with refined occupancies of 0.174 : 0.826. The disordered silver atom (Ag) in the cluster shell was split into two positions (Ag11/Ag2) with an occupancy ratio of 0.53 : 0.47. For the four Ag/Cu co-occupied sites: Three sites (Cu12/Ag15, Cu2/Ag17, and Cu13/Ag16) shared a common refinement variable, yielding a uniform Cu : Ag = 0.654 : 0.346; The fourth site (Cu14/Ag18) was independently refined to Cu : Ag = 0.846 : 0.154. Geometrical restraints were applied to maintain reasonable bond lengths, and anisotropic displacement parameters (ADPs) were constrained using SIMU and RIGU instructions to ensure physically reasonable thermal motion.

Refinement Details of $(AgCu)_{14}$-2: Sulfur atom disorder (S10A/S10B) in the cluster shell was modeled with an occupancy ratio of 0.53 : 0.47. The four Ag/Cu co-occupied sites refined to: Ag12/Cu4 = 0.137 : 0.863, Ag14/Cu1 = 0.08 : 0.92, Ag15/Cu3 = 0.133 : 0.867, and Ag13/Cu2 = 0.113 : 0.887. The $P(Ph\text{-}m\text{-}OMe)_3$ ligand and bonded Ag atoms (Ag5/Ag9) exhibited two-directional disorder with an occupancy ratio of 0.638 : 0.362. Geometrical constraints ensured reasonable bond lengths, and the EADP directive was applied to Ag5/Ag9. Geometrical restraints were applied to maintain reasonable bond lengths and angles, and anisotropic

displacement parameters (ADPs) were constrained using SIMU and RIGU instructions to ensure physically reasonable thermal motion.

CCDC codes: Detailed crystal data for **Ag_{14}**, **$(AgCu)_{14}$-1**, and **$(AgCu)_{14}$-2** NCs are given in Tables S1, S2, and S3, respectively. CCDC 2413802 for **Ag_{14}**, CCDC 2413803 for **$(AgCu)_{14}$-1**, and CCDC 2413801 for **$(AgCu)_{14}$-2** contain the supplementary crystallographic data for this paper. These data are provided free of charge by the Cambridge Crystallographic Data Centre.

III. Electrochemical measurements

To explore the effect of the increase in the number of Cu atoms in catalysis, we conducted eCO_2RR. The catalyst sample was prepared by loading NCs onto Ketjen Carbon (C) at a mass ratio of 1:1 (5 mg NC and 5 mg C), which was subsequently dispersed in isopropyl alcohol at a concentration of 2.5 $mg \cdot mL^{-1}$ under sonication for 10 mins. The final catalyst ink was prepared by thoroughly mixing 1 mL of catalyst suspension with 10 μL of Nafion (5 wt.%). Working electrodes were fabricated by casting 40 μL of this ink onto the effective contact area (2 × 0.5 cm^2) of carbon paper (2 × 1.5 cm^2), which was subsequently dried at room temperature. 1 M KOH solution (pH = 14). All electrochemical tests were carried out in a customized flow cell. The electrochemical performance of three catalysts on a gas diffusion electrode (GDE, 2 × 1.5 cm^2) was tested in a flow cell reactor. The three NC-coated carbon paper with a microporous layer (Sigracet 29 BCE, Fuel Cell Store) was applied as the GDE cathode. Hg/HgO in 1.0 M KOH saturated aqueous electrolyte was employed as the reference electrode. During the measurement process, the flow rate of CO_2 into the cathode GDE was 20 $mL \cdot min^{-1}$, and the flow rate of the cathode liquid (1 M KOH) was 40 rpm, which was controlled by a peristaltic pump (Cole-Parmer). The electroreduction CO_2 testing was carried out using the potentostat of Donghua DH7001B. The gaseous products in the electrochemical CO_2 reduction reaction were detected by gas chromatography (GC), and the liquid products were detected by ^1H NMR.

$E(RHE) = E(Hg/HgO) + 0.098 + 0.0592 * 14$

The faradaic efficiency (FE_X) and partial current density (j_X) of X (X= CO or H_2) were calculated as below:

$$FE_X = \frac{(N_i \times n \times F)}{Q_t}$$

$$j_X = \frac{FE_X \times Q_t}{t \times \text{Area}}$$

Where

Q_t = total charge consumed in the electrochemical reaction.

N_i = the number of moles of the product (measured by GC).

n = the number of electrons transferred in the elementary reaction (n is 2 for CO and H_2).

F = the Faradaic constant (96485 C mol^{-1}).

t = reaction time (s).

Area = geometry area of the electrode (1 cm^2).

At each potential, 400 μL of the electrolyzed catholyte was collected, and 200 μL of D_2O containing DMSO as an internal standard was added. The product peak area was calculated using software, and the Faraday efficiency (FE_{liquid}) of the liquid product was calculated using the following formula:

$$n_{formate} = \frac{n_{DMSO} \times n_1 \times S_1}{n_2 \times S_2}$$

$$FE_{formate} = \frac{n_{foemate} \times F \times n}{Q_t \times n_3} \times 100\%$$

Where

n_{DMSO} = The amount of the substance of the internal standard DMSO (0.00063 mmol).

n_1 = Amount of methyl ($-CH_3$) hydrogen on dimethyl sulfoxide ($n_1 = 6$).

n_2 = The amount of hydrogen in the liquid product.

n_3 = The ratio of cathode reaction solution to total catholyte taken when configuring ^1H NMR ($n_3 = 0.01$).

S_1 = Software calculates the liquid peak area based on the DMSO peak area.

S_2 = The DMSO peak area in the software is set to 1.

F = the Faradaic constant (96485 C mol^{-1}).

n = the number of electrons transferred in the elementary reaction.

Q_t = total charge consumed in the electrochemical reaction.

After the eCO_2RR tests were completed, the samples were rinsed with CH_2Cl_2 and collected for UV-vis characterization.

IV. DFT calculations

Periodic DFT calculations were performed with the VASP code using the Perdew-Burke-Ernzerhof exchange-correlation function of the generalized gradient approximation (GGA). Projector augmented wave (PAW) pseudopotential was used to describe core-valence interactions, with [Ag]-$5s^14d^{10}$ and [Cu]-$4s^13d^{10}$ as valence electrons. The plane-wave cutoff energy was set to 400 eV. The Brillouin zone of the reciprocal space was sampled with the Γ-centred Monkhorst-Pack scheme, the k-point mesh was set to 1 × 1 × 1 for the geometry optimization. The energy convergence of the self-consistent iteration reached 10^{-5} eV per atom, and the Hermann-Feynman force convergence was 0.03 eV $Å^{-1}$, ensuring that the structure optimization process converged to a stable structure.

The computational hydrogen electrode (CHE) model was used to calculate the Gibbs free energy of the electrochemical and non-electrochemical elementary steps involved in ECR, defined as:

$$\Delta G = \Delta E - T\Delta S + \Delta ZPE$$

Here, ΔE is the difference in the total energy of the reaction of the elementary steps as calculated by the DFT in vacuum. TΔS and ΔZPE are the entropy and zero-point energy changes at 298.15 K, respectively.

Section 2. Supporting Figures

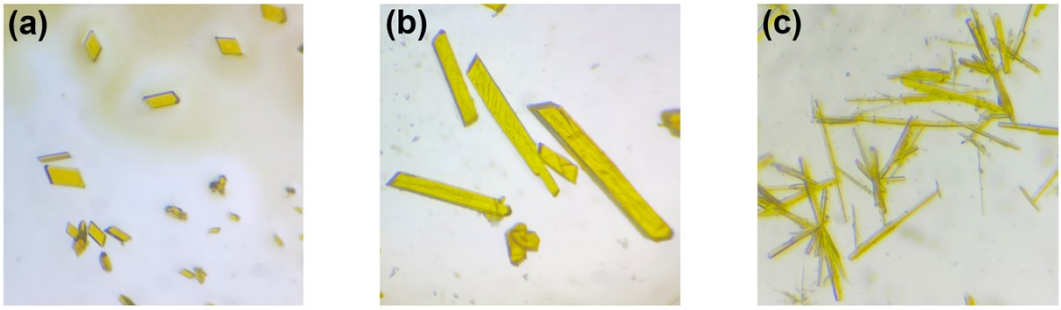

Fig. S1 The optical microscopic image of the single crystals of **Ag_{14}**, **$(AgCu)_{14}$-1**, and **$(AgCu)_{14}$-2** NCs. (a) **Ag_{14}**; (c) **$(AgCu)_{14}$-1**; (c) **$(AgCu)_{14}$-2**.

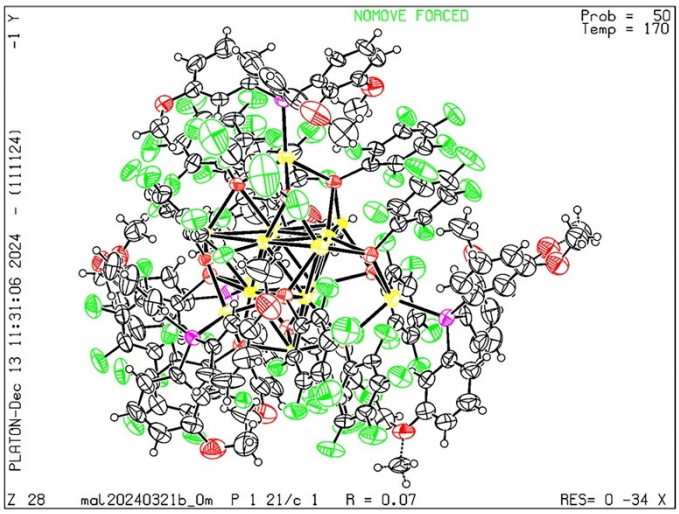

Fig. S2 The thermal ellipsoids of the ORTEP diagram of the **Ag_{14}** cluster.

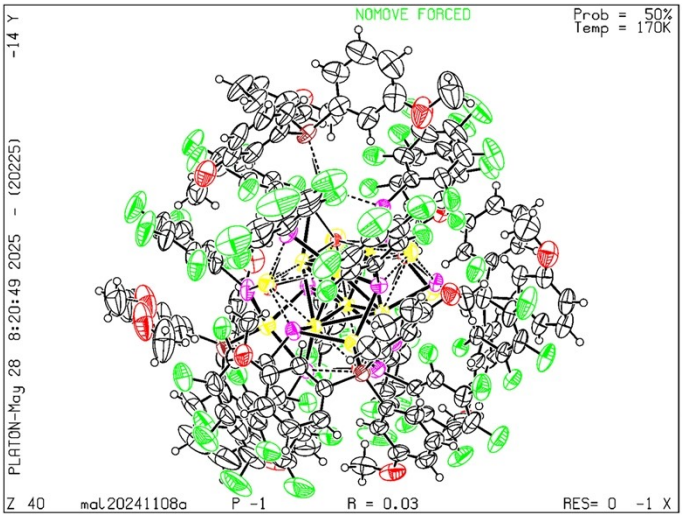

Fig. S3 The thermal ellipsoids of the ORTEP diagram of the **$(AgCu)_{14}$-1** cluster.

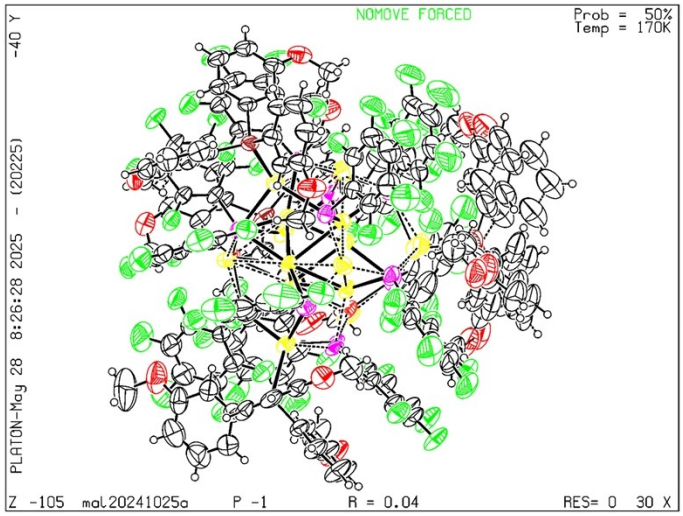

Fig. S4 The thermal ellipsoids of the ORTEP diagram of the **$(AgCu)_{14}$-2** cluster.

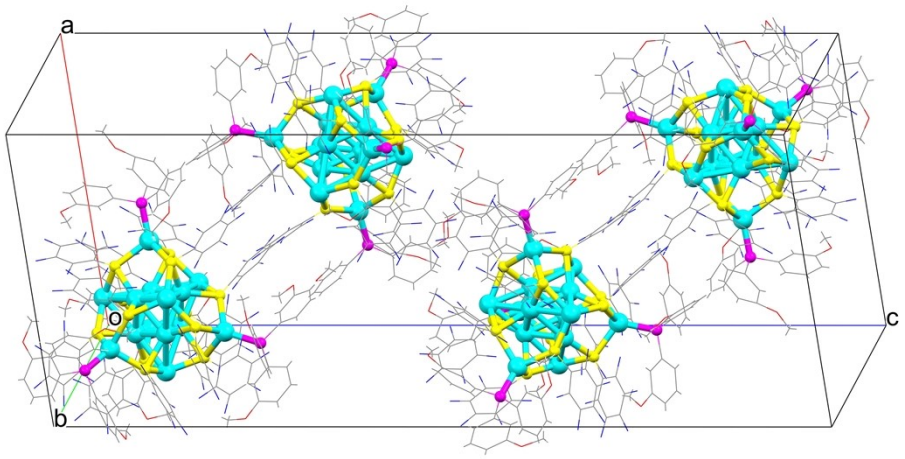

Fig. S5 The presence of four **Ag_{14}** cluster molecules in a unit cell. Color labels: turquoise = Ag; yellow = S; magenta = P; blue = F; pink = O; grey = C; white = H.

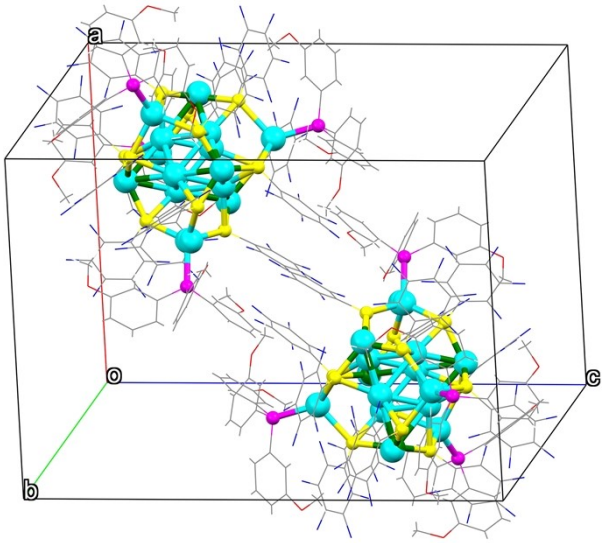

Fig. S6 The presence of two **$(AgCu)_{14}$-1** cluster molecules in a unit cell. Color labels: turquoise = Ag; green = Cu; yellow = S; magenta = P; blue = F; pink = O; grey = C; white = H.

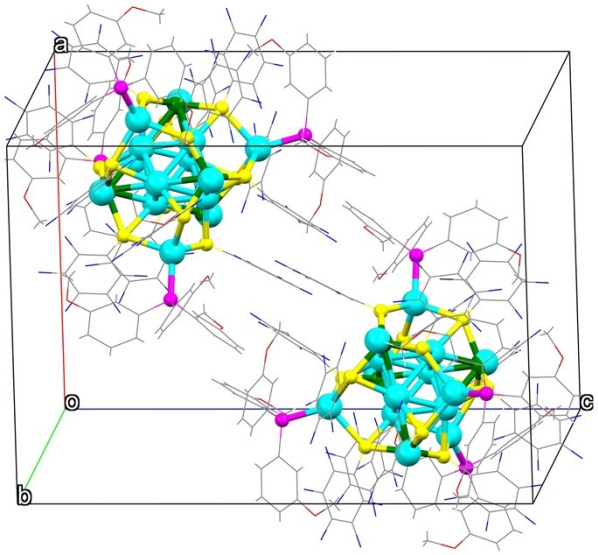

Fig. S7 The presence of two **$(AgCu)_{14}$-2** cluster molecules in a unit cell. Color labels: turquoise = Ag; green = Cu; yellow = S; magenta = P; blue = F; pink = O; grey = C; white = H.

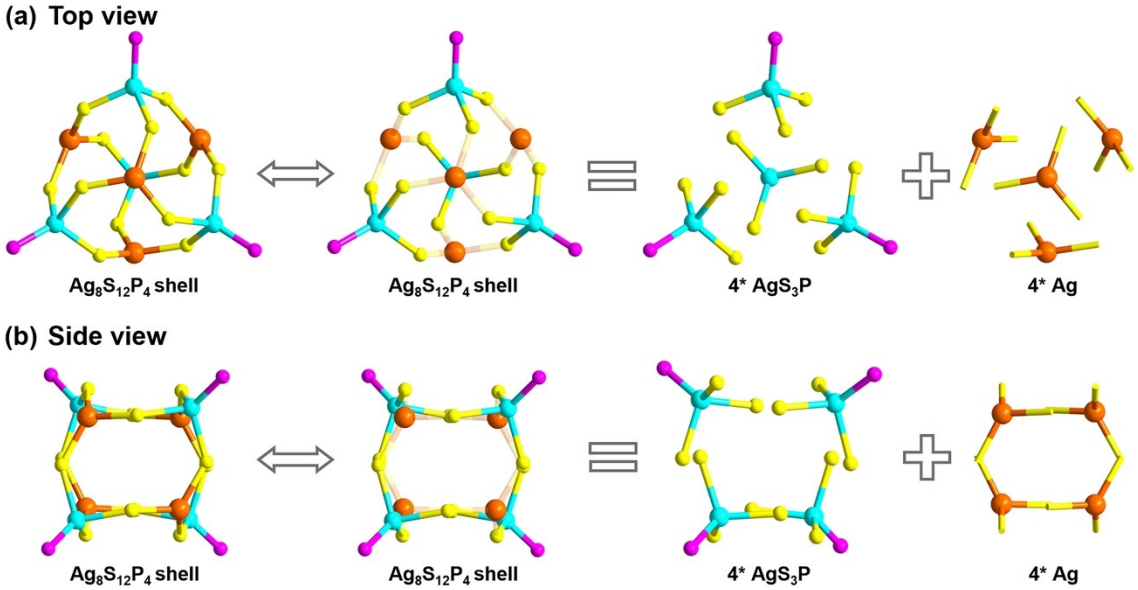

Fig. S8 Structural analysis of $Ag_8S_{12}P_4$ shell. (a) and (b) Top and side views of the $Ag_8S_{12}P_4$ shell consisting of four AgS_3P motifs and four Ag atoms. Color labels: turquoise/orange = Ag; yellow = S; magenta = P.

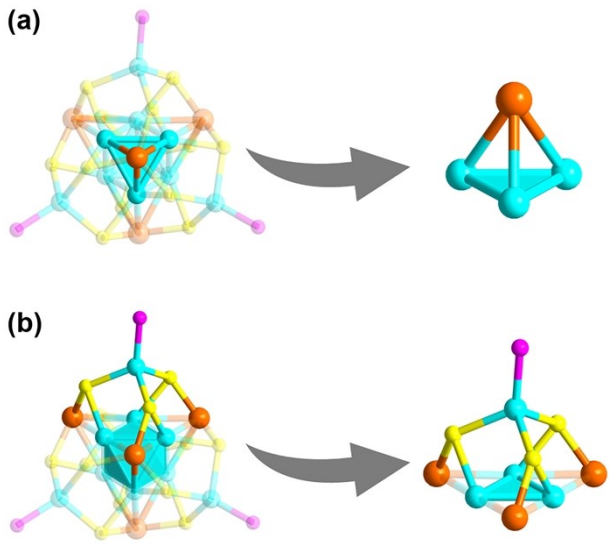

Fig. S9 The coordination modes of Ag atoms in **Ag_{14}** NC. (a) The μ_3 (Ag, Ag, Ag, Ag) coordination modes of four Ag atoms on the core surface of the Ag_6 core. (b) The μ_2 (S, Ag, Ag) coordination modes of twelve S atoms on the core surface of the Ag_6 core. Color labels: turquoise/orange = Ag; yellow = S; magenta = P.

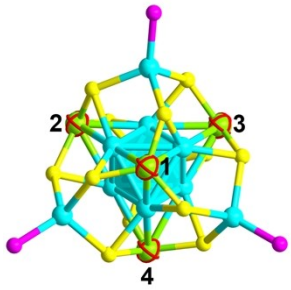

	$(AgCu)_{14}$-1		$(AgCu)_{14}$-2	
Site	Ag%	Cu%	Ag%	Cu%
1	34.6%	65.4%	13.3%	86.7%
2	15.4%	84.6%	11.3%	88.7%
3	34.6%	65.4%	13.7%	86.3%
4	34.6%	65.4%	8.0 %	92.0 %
Total metal atoms	1.192	2.808	0.463	3.537

Fig. S10 The occupancy information of metal sites 1-4 in **$(AgCu)_{14}$-1** and **$(AgCu)_{14}$-2** NCs. Color labels: turquoise = Ag; light green = Ag/Cu; yellow = S; magenta = P.

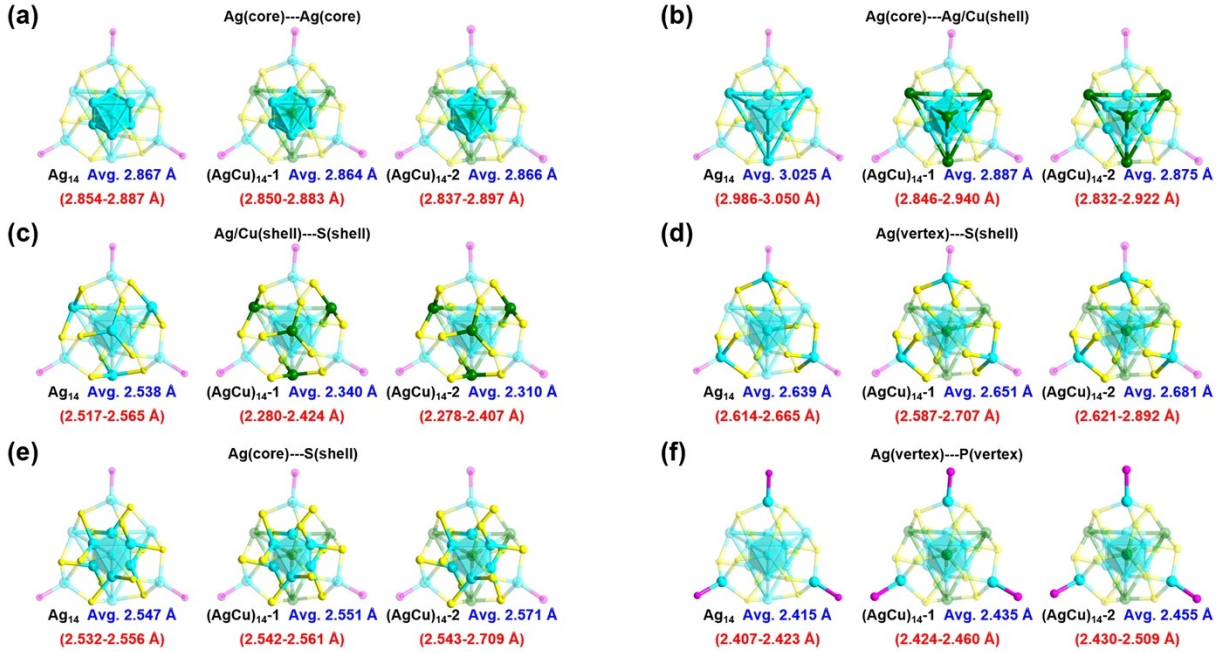

Fig. S11 Structural comparison and bond length among **Ag_{14}**, **$(AgCu)_{14}$-1**, and **$(AgCu)_{14}$-2** NCs. (a) Comparison of the bond length of Ag(core)---Ag(core); (b) Comparison of the bond length of Ag(core)---Ag/Cu(shell); (c) Comparison of the bond length of Ag/Cu(shell)---S(shell); (d) Comparison of the bond length of Ag(vertex)---S(shell); (e) Comparison of the bond length of Ag(core)---S(shell); (f) Comparison of the bond length of Ag(vertex)---P(vertex). Color labels: turquoise = Ag; green = Cu; yellow = S; magenta = P. The introduction of Cu alters bond lengths in the **Ag_{14}** NC. Specifically, we analyzed bond lengths involving Cu at the four disordered sites. The average Ag-Ag distance in the Ag_6 core is 2.867, 2.864, and 2.866 Å, slightly shorter than the 2.889 Å in bulk silver, indicating strong interactions between the core Ag (Fig. S11a). After Cu incorporation, the Ag-Ag/Cu bond lengths between shell Ag/Cu atoms and core Ag atoms decrease from 3.025 Å in **Ag_{14}** to 2.887 Å in **$(AgCu)_{14}$-1**, and 2.875 Å in **$(AgCu)_{14}$-2**, due to Cu's smaller radius (Fig. S11b). The Ag/Cu-S bond lengths between shell Ag/Cu atoms and the S atoms in the AgS_3P unit also decrease from 2.538 Å in **Ag_{14}** to 2.310 Å in **$(AgCu)_{14}$-2** (Fig. S11c). Cu doping also further affects both the metal-thiolate and the P-metal bond distances (Fig. S11d-f). For example, in **$(AgCu)_{14}$-2**, the P-Ag distance is 2.455 Å, longer than 2.435 Å in **$(AgCu)_{14}$-1** and 2.415 Å in **Ag_{14}**.

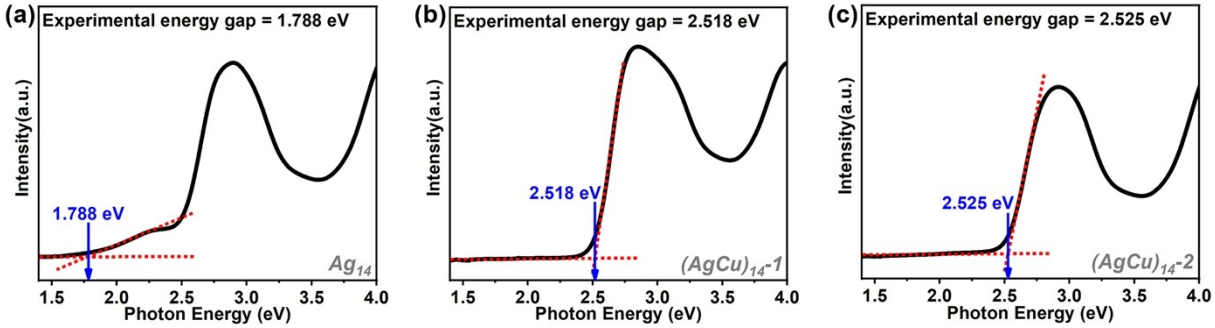

Fig. S12 UV-vis absorption spectra (photon energy scale) of the **Ag_{14}**, **$(AgCu)_{14}$-1**, and **$(AgCu)_{14}$-2** NCs in CH_2Cl_2. (a) **Ag_{14}**; (b) **$(AgCu)_{14}$-1**; (c) **$(AgCu)_{14}$-2**. The experimental energy gap of the **Ag_{14}**, **$(AgCu)_{14}$-1**, and **$(AgCu)_{14}$-2** NCs in CH_2Cl_2 was determined as ~1.788 eV, 2.518 eV, and 2.525 eV, respectively.

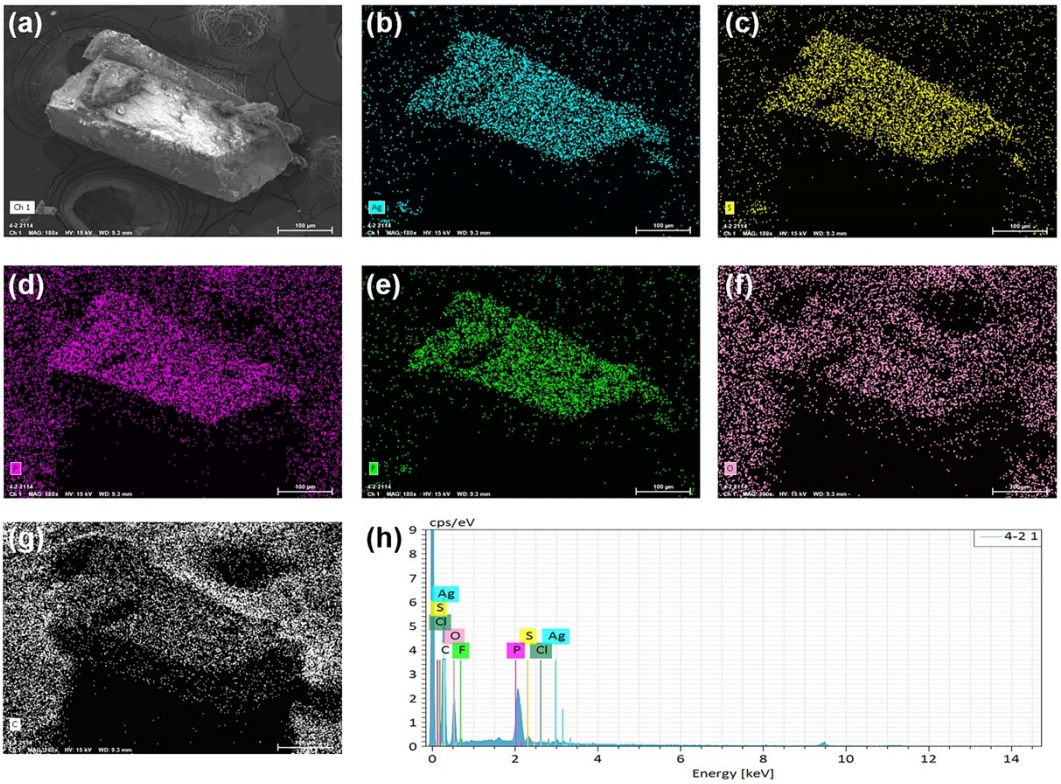

Fig. S13 SEM image and corresponding elemental mapping images of the **Ag_{14}** crystals. (a) SEM image of single crystal; (b)-(g) Elemental mapping images of Ag, S, P, F, O, and C elements, respectively; (h) EDS spectrum confirming the presence of above elements (Ag, S, P, F, O, and C) in **Ag_{14}** NC.

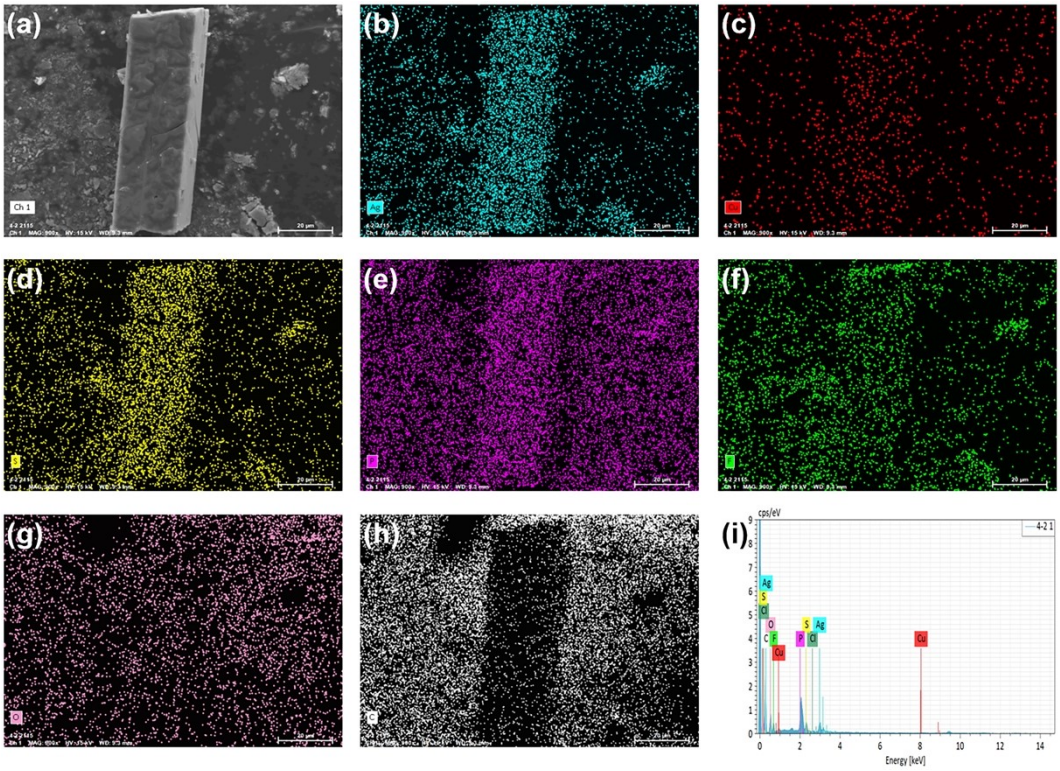

Fig. S14 SEM image and corresponding elemental mapping images of the **$(AgCu)_{14}$-1** crystals. (a) SEM image of single crystal; (b)-(h) Elemental mapping images of Ag, Cu, S, P, F, O, and C elements, respectively; (i) EDS spectrum confirming the presence of above elements (Ag, Cu, S, P, F, O, and C) in **$Ag_{12}Cu_2$** NC.

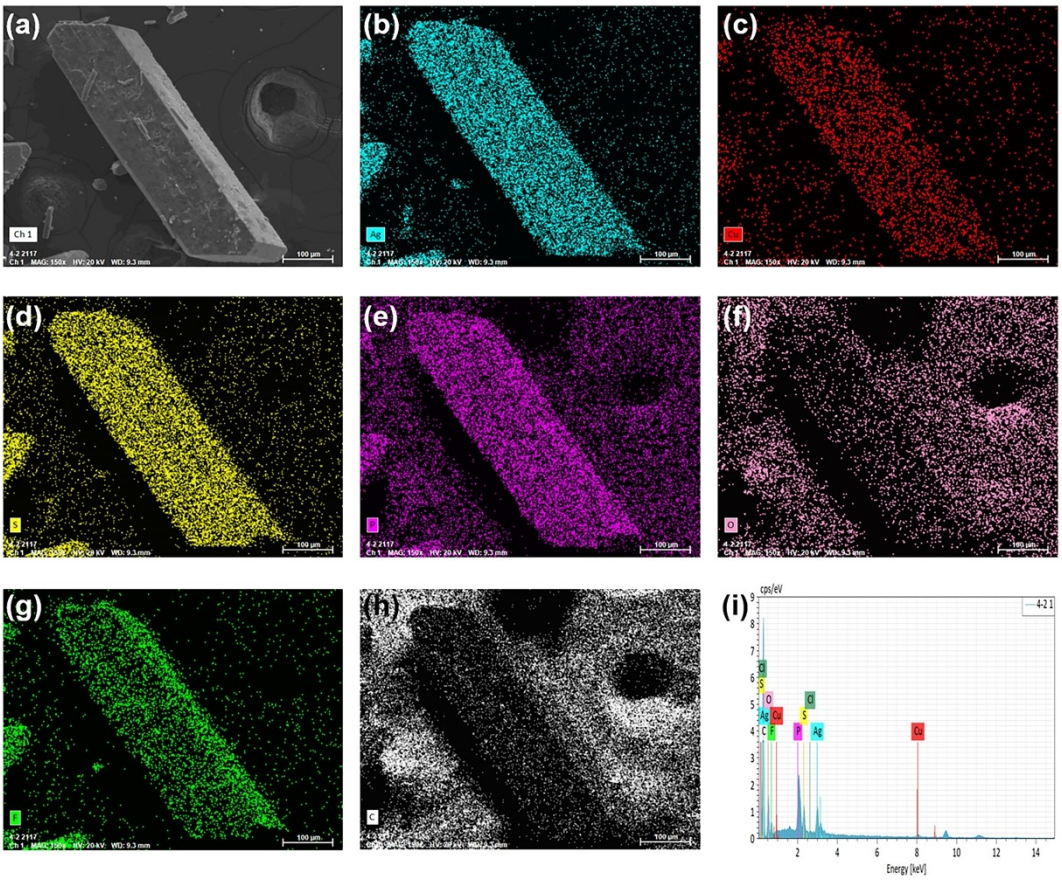

Fig. S15 SEM image and corresponding elemental mapping images of the **$(AgCu)_{14}$-2** crystals. (a) SEM image of single crystal; (b)-(h) Elemental mapping images of Ag, Cu, S, P, F, O, and C elements, respectively; (i) EDS spectrum confirming the presence of above elements (Ag, Cu, S, P, F, O, and C) in **$Ag_{10}Cu_4$** NC.

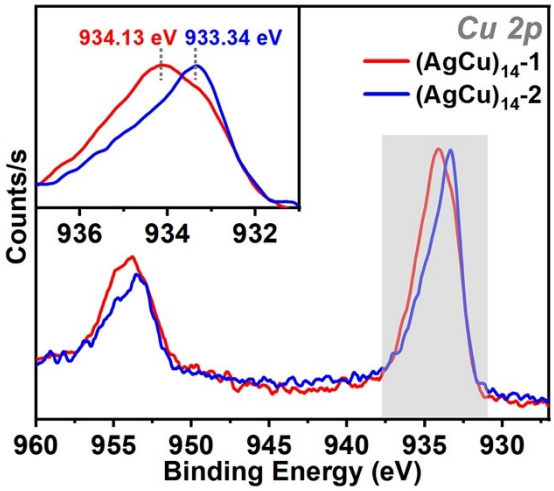

Fig. S16 Cu 2p spectra of **$(AgCu)_{14}$-1** (red) and **$(AgCu)_{14}$-2** (blue) NCs. Insets: photographs of the corresponding partial enlargement.

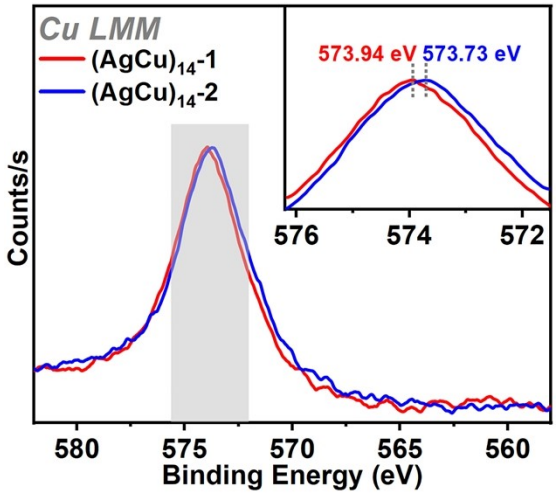

Fig. S17 The Cu LMM Auger spectra of the **$(AgCu)_{14}$-1** (red) and **$(AgCu)_{14}$-2** (blue) NCs. Insets: photographs of the corresponding partial enlargement.

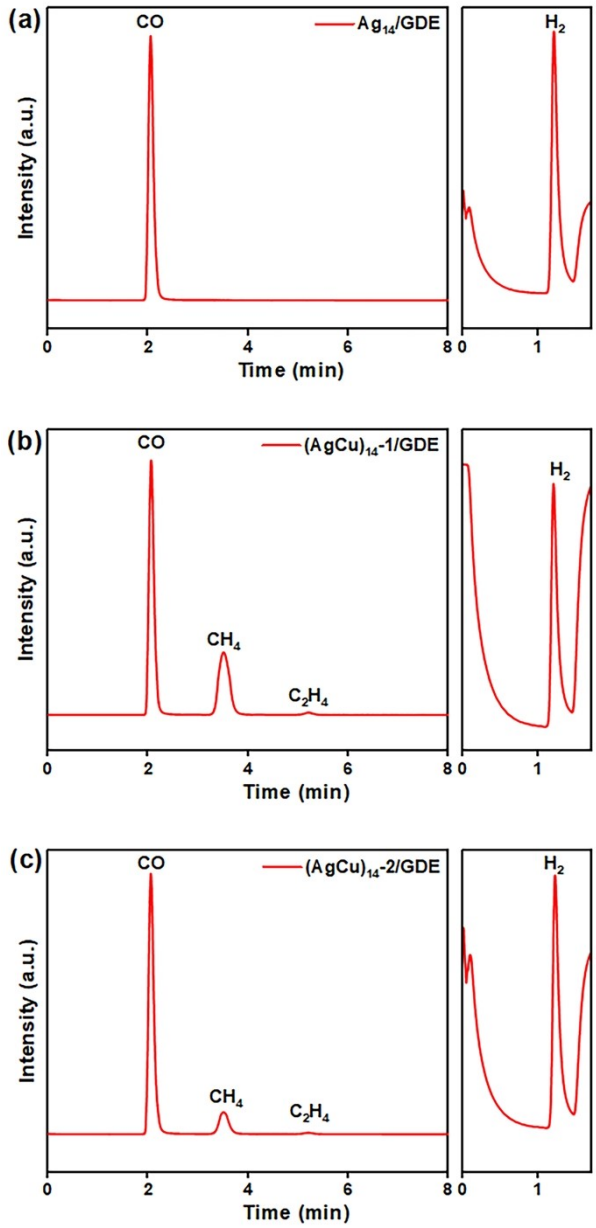

Fig. S18 Gas products (CO, CH_4, C_2H_4, and H_2) analysis for eCO_2RR on (a) **Ag_{14}/GDE**, (b) **$(AgCu)_{14}$-1/GDE**, and (c) **$(AgCu)_{14}$-2/GDE**. Gas chromatography showing the gas products of eCO_2RR at –1.6 V vs. RHE.

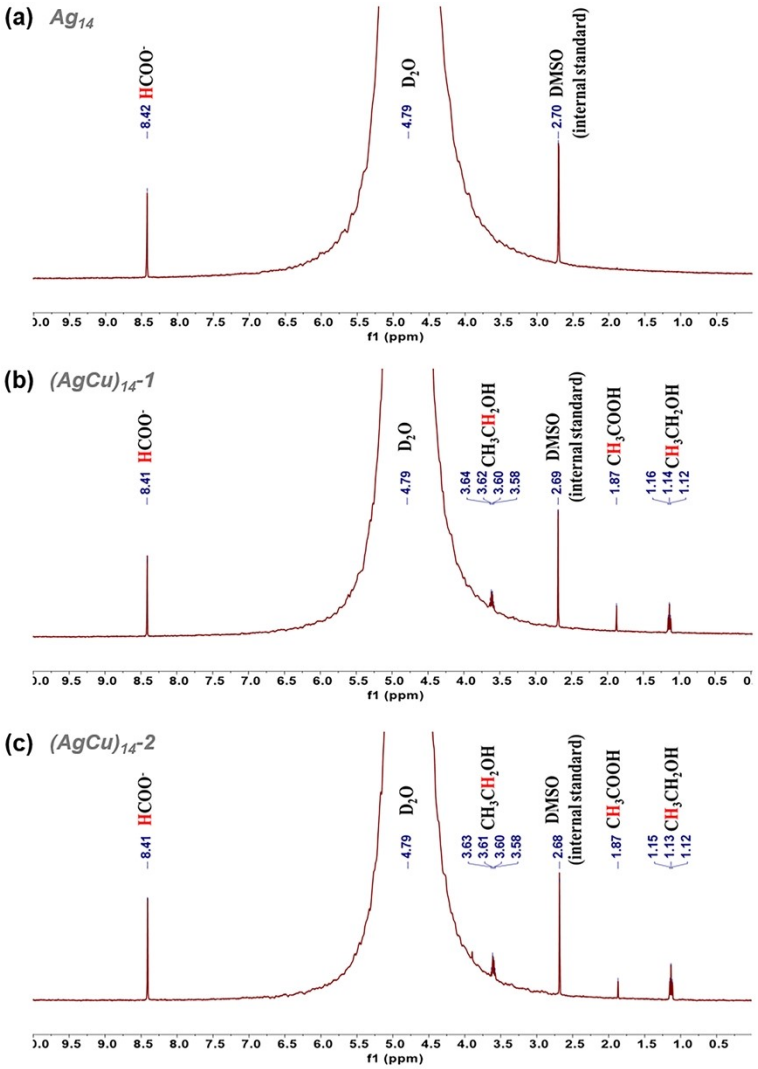

Fig. S19 ^{1}H-NMR spectral data of liquid products for the **Ag_{14}/GDE**, **$(AgCu)_{14}$-1/GDE**, and **$(AgCu)_{14}$-2/GDE** catalysts. (a) **Ag_{14}/GDE**; (b) **$(AgCu)_{14}$-1/GDE**; (c) **$(AgCu)_{14}$-2/GDE**.

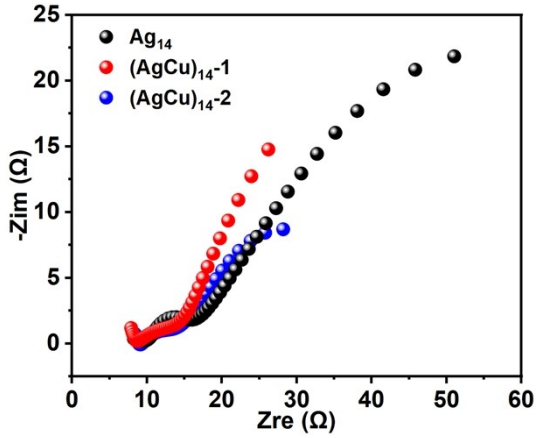

Fig. S20 Electrochemical impedance spectra of the **Ag_{14}/GDE**, **$(AgCu)_{14}$-1/GDE**, and **$(AgCu)_{14}$-2/GDE** catalysts.

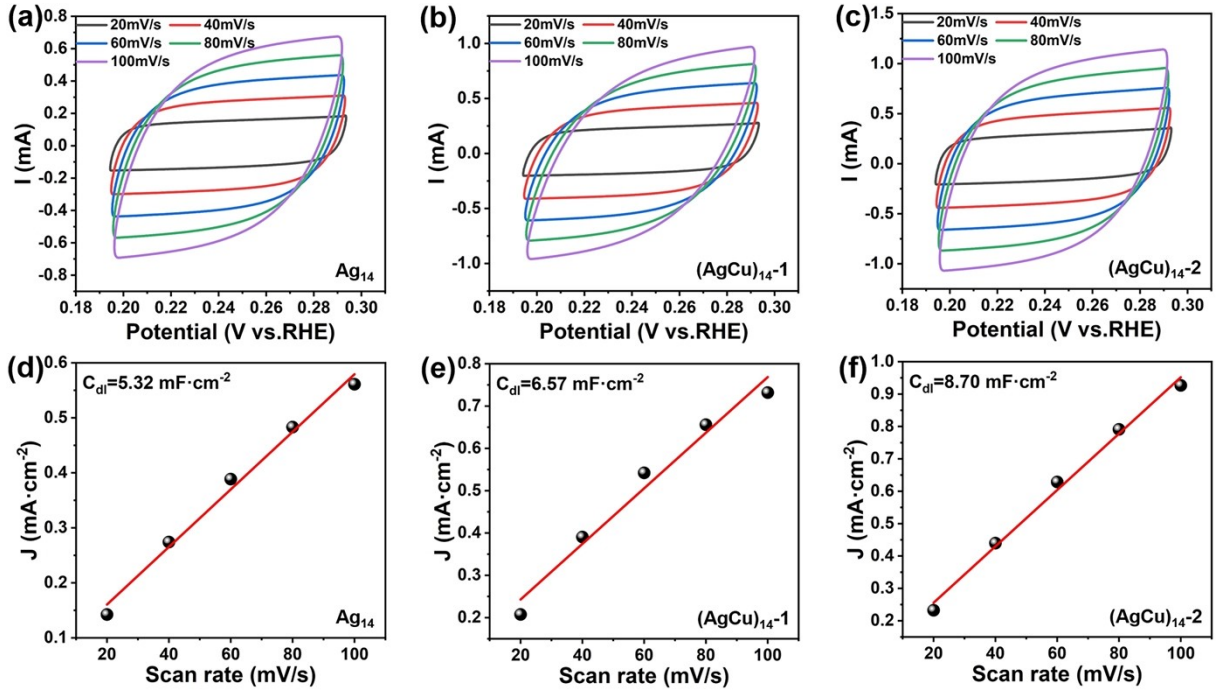

Fig. S21 Cyclic voltammetry of (a) **Ag_{14}/GDE**, (b) **$(AgCu)_{14}$-1/GDE**, and (c) **$(AgCu)_{14}$-2/GDE** catalysts in 1 M KOH electrolyte at a scan rate from 20, 40, 60, 80, and 100 $mV \cdot s^{-1}$; The corresponding linear curves of current density and scan rate of (d) **Ag_{14}/GDE**, (e) **$(AgCu)_{14}$-1/GDE**, and (f) **$(AgCu)_{14}$-2/GDE** catalysts.

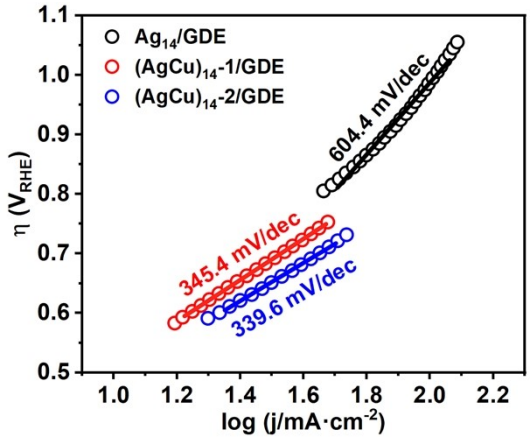

Fig. S22 Tafel plots constructed for the eCO_2RR on the three catalysts.

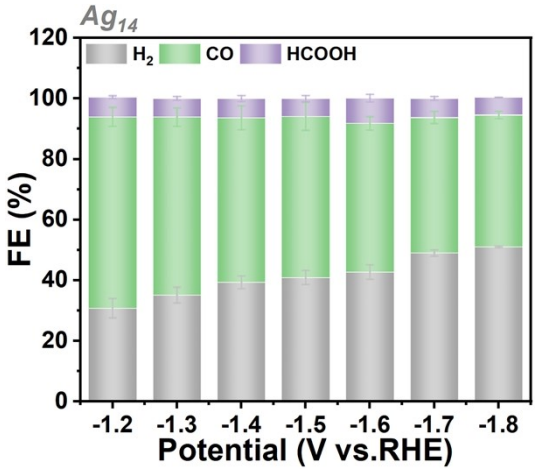

Fig. 23 FEs for various eCO_2RR products obtained on **Ag_{14}/GDE** catalyst in a 1 M KOH solution.

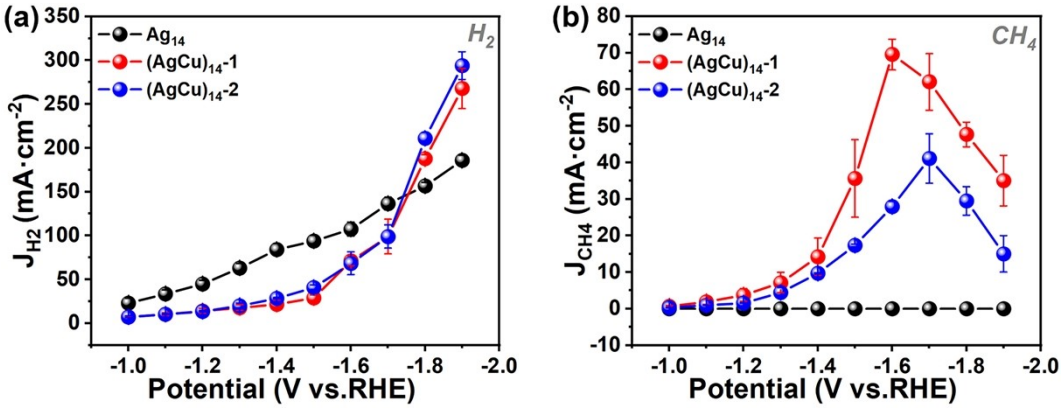

Fig. S24 H_2 and CH_4 partial current density of the **Ag_{14}/GDE** (black), **$(AgCu)_{14}$-1/GDE** (red), and **$(AgCu)_{14}$-2/GDE** (blue) catalysts at different potentials. (a) H_2; (b) CH_4.

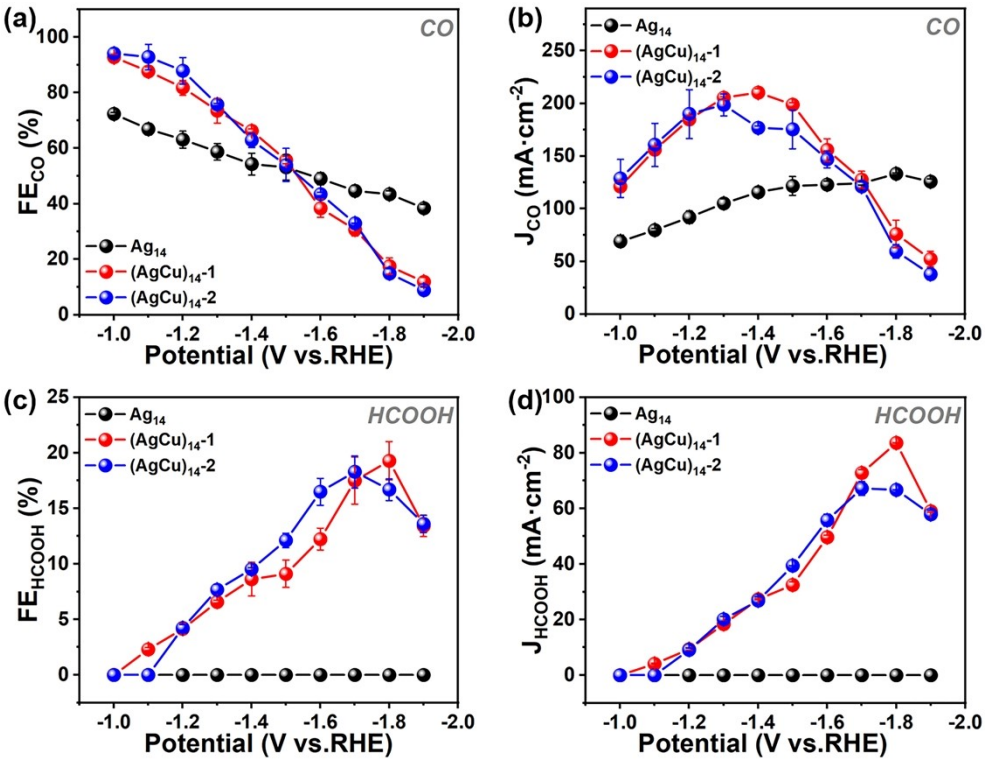

Fig. S25 CO and HCOOH faradaic efficiency and partial current density of the **Ag_{14}/GDE** (black), **$(AgCu)_{14}$-1/GDE** (red), and **$(AgCu)_{14}$-2/GDE** (blue) catalysts at different potentials. (a) CO faradaic efficiency; (b) CO partial current density; (c) HCOOH faradaic efficiency; (d) HCOOH partial current density.

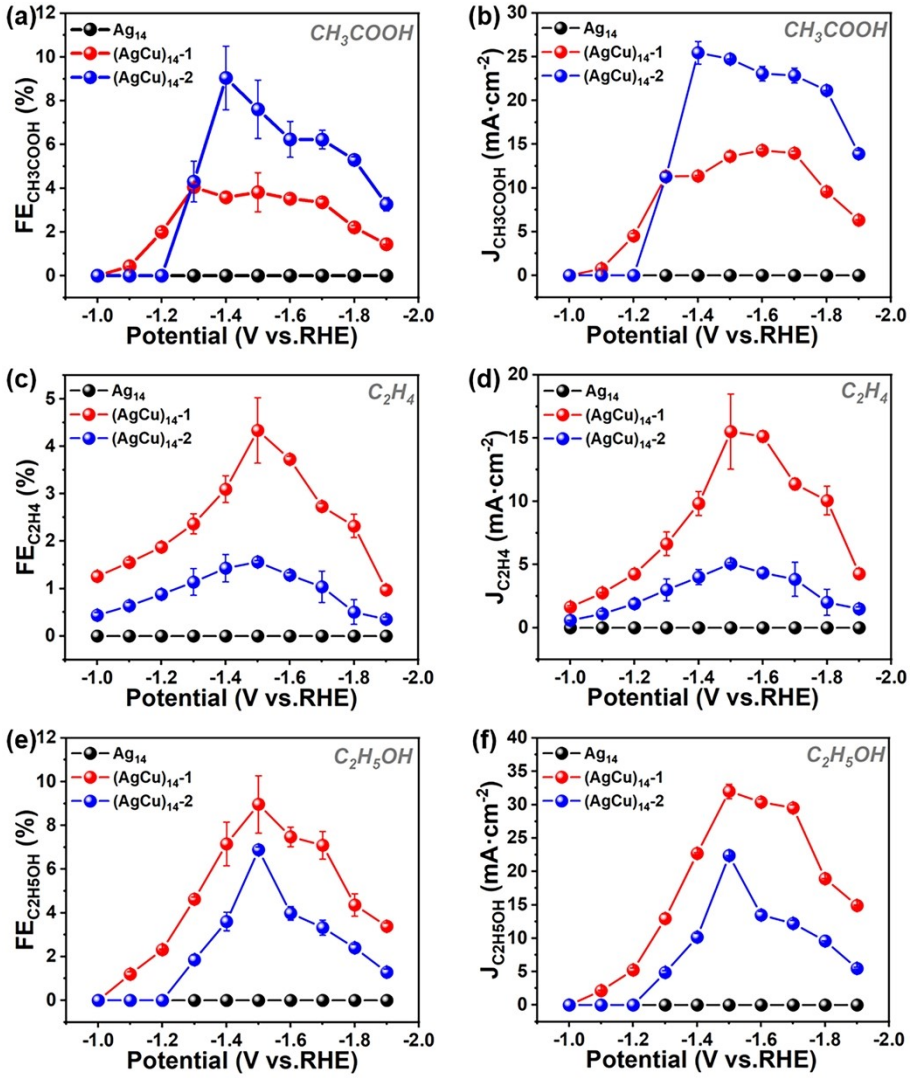

Fig. S26 CH_3COOH, C_2H_4, and C_2H_5OH faradaic efficiency and partial current density of the **Ag_{14}/GDE** (black), **$(AgCu)_{14}$-1/GDE** (red), and **$(AgCu)_{14}$-2/GDE** (blue) catalysts at different potentials. (a) CH_3COOH faradaic efficiency; (b) CH_3COOH partial current density; (c) C_2H_4 faradaic efficiency; (d) C_2H_4 partial current density; (e) C_2H_5OH faradaic efficiency; (f) C_2H_5OH partial current density.

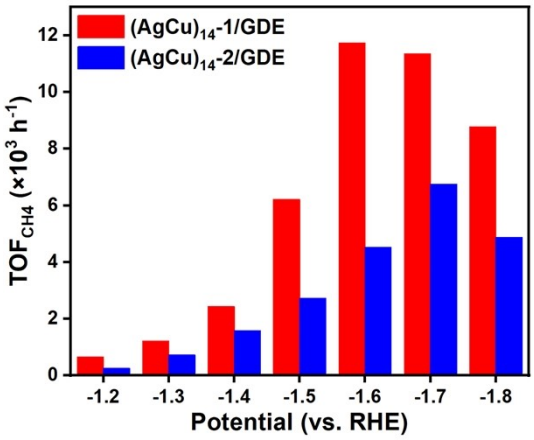

Fig. S27 The turnover frequency of CH_4 products was obtained from **$(AgCu)_{14}$-1/GDE** and **$(AgCu)_{14}$-2/GDE.**

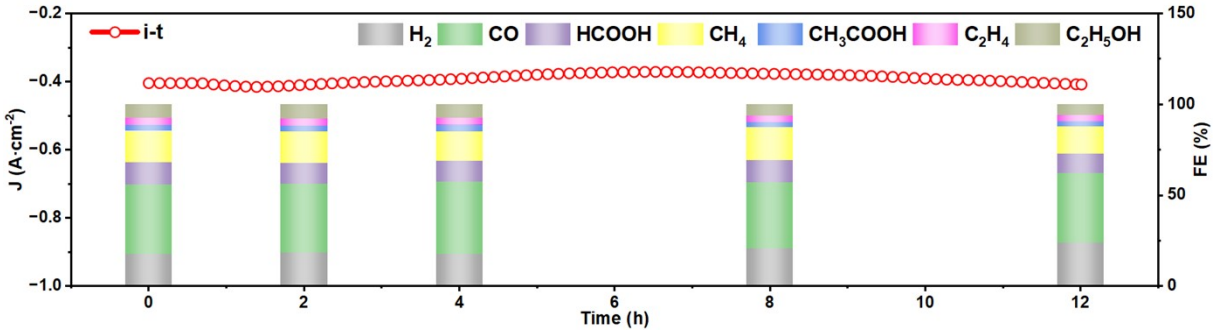

Fig. S28 Catalytic stability of **$(AgCu)_{14}$-1/GDE** at –1.6 V vs. RHE for 12 h, (top) *i*-t curve; (bottom) selectivity of various eCO_2RR products at different time.

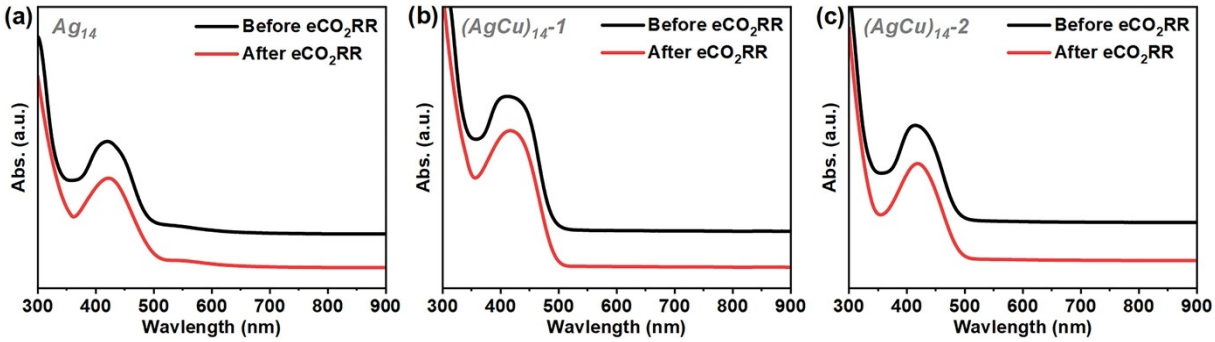

Fig. S29 UV-vis absorbance spectra of the **Ag_{14}**, **$(AgCu)_{14}$-1**, and **$(AgCu)_{14}$-2** NCs before and after eCO_2RR. (a) **Ag_{14}**; (b) **$(AgCu)_{14}$-1**; (c) **$(AgCu)_{14}$-2**.

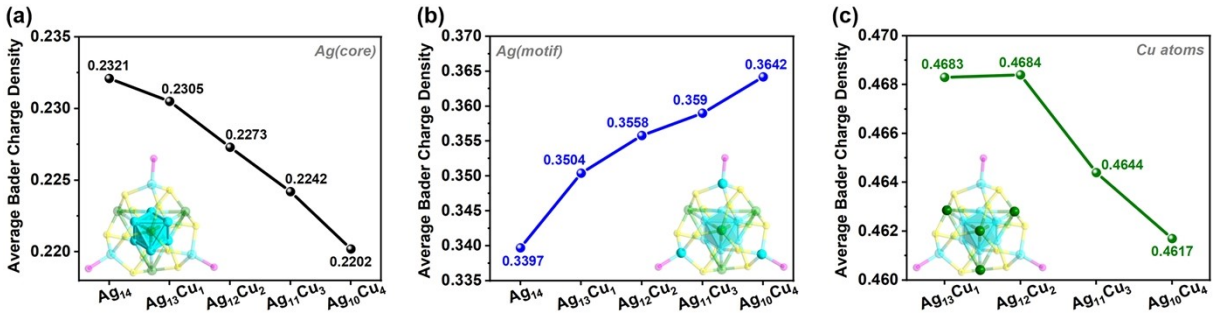

Fig. S30 The average Bader charge densities of the Ag atoms in Ag_6 core, the Ag atoms in AgS_3P motifs, and the Cu atoms of the $\mathbf{Ag_{14-x}Cu_x}$ (x=0-4) structure. (a) Ag(core); (b) Ag(motif); (c) Cu atoms. Color labels (as illustrated by the $Ag_{10}Cu_4$ structure): turquoise = Ag; green = Ag/Cu; yellow = S; magenta = P.

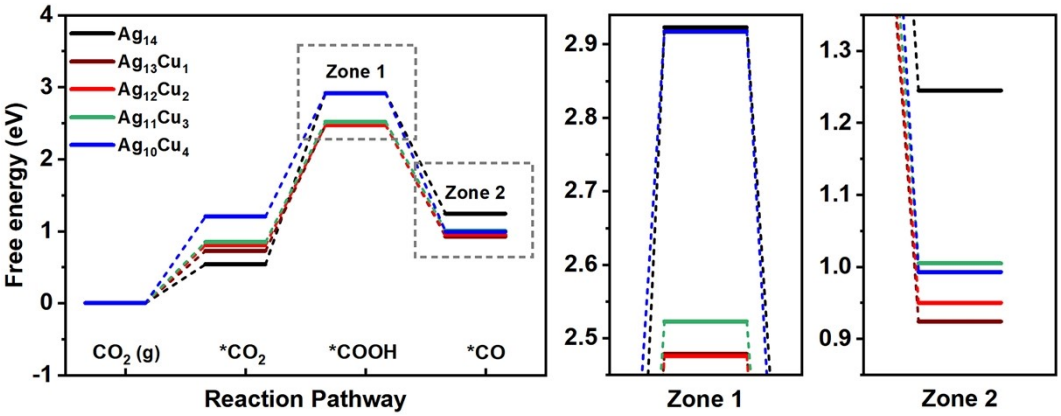

Fig. S31 Calculated the free energy diagram for $*CO_2$, *COOH, and *CO intermediates on the $\mathbf{Ag_{14-x}Cu_x}$ (x = 0/1/2/3/4).

Section 3. Supporting Table

Table S1 The crystal structure parameters for **Ag_{14}**.

Empirical formula	$C_{156}H_{84}Ag_{14}F_{60}O_{12}P_4S_{12}$
Formula weight	5481.40
Temperature/K	170
Crystal system	monoclinic
Space group	$P2_1/c$
a/Å	19.3202(8)
b/Å	19.1149(7)
c/Å	27.840(19)
α/°	90
β/°	95.3950(10)
γ/°	90
Volume/Å^3	18082.2(13)
Z	4
ρ_{calc}g/cm^3	2.013
μ/mm^{-1}	1.803
F(000)	10629.0
Radiation	Mo Kα (λ = 0.71073)
2Θ range for data collection/°	3.772 to 50
Index ranges	$-22 \leq h \leq 22$, $-22 \leq k \leq 21$, $-58 \leq l \leq 58$
Reflections collected	191046
Independent reflections	31803 [R_{int} = 0.0503, R_{sigma} = 0.0421]
Data/restraints/parameters	31803/3973/2341
Goodness-of-fit on F^2	1.197
Final R indexes [I>=2σ (I)]	R_1 = 0.0695, wR_2 = 0.1524
Final R indexes [all data]	R_1 = 0.0863, wR_2 = 0.1566
Largest diff. peak/hole / e Å^{-3}	1.01/-0.89

Table S2 The crystal structure parameters for **$(AgCu)_{14}$-1**.

Empirical formula	$C_{165}H_{113}Ag_{11.192}Cl_7Cu_{2.808}F_{60}O_{17.5}P_4S_{12}$
Formula weight	5658.0
Temperature/K	170
Crystal system	triclinic
Space group	$P\bar{1}$
a/Å	18.7706(7)
b/Å	19.9187(9)
c/Å	25.5916(12)
α/°	89.783(2)
β/°	88.6660(10)
γ/°	87.6930(10)
Volume/Å^3	9558.0(7)
Z	2
ρ_{calc}g/cm^3	1.966
μ/mm^{-1}	1.804
F(000)	5523.0
Radiation	Mo Kα (λ = 0.71073)
2Θ range for data collection/°	3.896 to 51
Index ranges	$-22 \leq h \leq 22$, $-24 \leq k \leq 24$, $-30 \leq l \leq 30$
Reflections collected	309839
Independent reflections	35550 [R_{int} = 0.0665, R_{sigma} = 0.0339]
Data/restraints/parameters	35550/4178/2389
Goodness-of-fit on F^2	1.053
Final R indexes [I>=2σ (I)]	R_1 = 0.0344, wR_2 = 0.0842
Final R indexes [all data]	R_1 = 0.0514, wR_2 = 0.0907
Largest diff. peak/hole / e Å^{-3}	0.90/-0.74

Table S3 The crystal structure parameters for **$(AgCu)_{14}$-2**.

Empirical formula	$C_{160}H_{98}Ag_{10.463}Cl_2Cu_{3.537}F_{60}O_{15}P_4S_{12}$
Formula weight	5333.26
Temperature/K	170
Crystal system	triclinic
Space group	$P\bar{1}$
a/Å	18.7192(11)
b/Å	19.3113(13)
c/Å	25.7905(17)
α/°	89.531(2)
β/°	89.166(2)
γ/°	85.539(2)
Volume/Å^3	9293.6(10)
Z	2
ρ_{calc}g/cm^3	1.906
μ/mm^{-1}	1.786
F(000)	5197.0
Radiation	Mo Kα (λ = 0.71073)
2Θ range for data collection/°	3.814 to 50
Index ranges	$-22 \leq h \leq 22$, $-22 \leq k \leq 22$, $-30 \leq l \leq 30$
Reflections collected	193338
Independent reflections	32726 [R_{int}= 0.0454, R_{sigma}= 0.0315]
Data/restraints/parameters	32726/5032/2287
Goodness-of-fit on F^2	1.111
Final R indexes [I>=2σ (I)]	R_1= 0.0370, wR_2= 0.1016
Final R indexes [all data]	R_1= 0.0549, wR_2= 0.1087
Largest diff. peak/hole / e Å^{-3}	1.21/-0.69